Asian Journal of Chemistry; Vol. 35, No. 10 (2023), 2461-2467

ASIAN JOURNAL OF CHEMISTRY

https://doi.org/10.14233/ajchem.2023.28210

Synthesis and Characterization of Cobalt doped Zinc Ferrite for its Structural and Magnetic Properties

AVINASH CHAND YADAV[1], PRABHAT RANJAN TIWARI[1], GULAB SINGH[2], PARASMANI RAJPUT[3], MANVENDRA KUMAR[4] and SANTOSH KUMAR[1,*]

[1]Department of Physics, Faculty of Engineering & Technology, V.B.S. Purvanchal University, Jaunpur-222003, India
[2]Department of Physics, Feroze Gandhi College, Raebareli-229001, India
[3]Beamline Development and Application Section, Bhabha Atomic Research Centre, Trombay, Mumbai-400085, India
[4]Department of Physics, Shri Vaishnav Vidyapeeth Vishwavidyalaya, Indore-453111, India

*Corresponding author: E-mail: skumarpu@rediffmail.com

Received: 6 July 2023; *Accepted*: 10 August 2023; *Published online*: 28 September 2023; AJC-21397

In this work, the synthesis of cobalt doped zinc ferrites $Co_xZn_{1-x}Fe_2O_4$ for x = 0, 0.1, 0.2 and 0.3 by sol-gel method followed by self-ignition root is reported. The prepared materials in powder form were characterized by HRXRD, FTIR, SEM and VSM analysis for its structural, vibrational and magnetic properties. Single phase cubic structure having *fd3m* space group of the zinc ferrites was revealed by HRXRD technique. The minimum crystallite size of Co doped $ZnFe_2O_4$ was found to be 26.11 nm for x = 0.1. The effect of cobalt in the prepared composites was studied using VESTA and Match3! Software for the structural analysis. The FTIR spectra illustrate two bands in the range 565-544 cm^{-1} and 431-410 cm^{-1}, which confirm the formation of the spinel ferrite phase. Vibrating sample magnetometer (VSM) was used for magnetic parameters like remanence, coercivity and saturation magnetization, *etc.* of the prepared nanomaterials.

Keywords: Sol-gel, Auto combustion, Zinc ferrite, Cobalt ferrite.

INTRODUCTION

Study of magnetic nanoparticles has been cutting edge for a very long time. They are widely used in the production of high value items like magnetic recording media, random-access memory (RAM) and magnetic field sensors in the ever expanding electronic sector. Amazing physical and technical uses exist for magnetic materials of the ferrimagnetic class, especially cobalt-based ferrite materials [1-3]. Cobalt zinc ferrite has recently received interest on a global scale because of its superior electromagnetic characteristics and physical/chemical stability [4]. It can be employed as an active component in a variety of processes, including microwave absorption, super capacitive energy storage, magnetic record medium and catalysis [5-11].

New magnetic materials can also be advantageous for an emerging class of materials known as multiferroics, particularly for producing multiferroic composite materials [12-14]. The development of more intelligent technologies, which will be at the core of the future generation of sensors, actuators and switches in a variety of advances, particularly in the internet of things (IOT) domain, may be facilitated by the use of multiferroic materials. Ferrite has exceptional electrical and magnetic properties and a wide range of practical uses in magneto-caloric refrigeration, information storage systems, ferro-fluid technologies and medical diagnostics. Due to its strong cubic magneto-crystalline anisotropy, high coercivity and mild saturation magnetization, $CoFe_2O_4$ is one of the most intriguing spinel ferrites [15,16]. The curie temperature and chemical stability of hard magnetic Co-Zn are both quite high, thus it is helpful in high frequency magnetic applications, magnetic recording applications (audio-video cassettes), recording discs, high density digital, *etc.* due to its high electrical resistivity and negligible eddy current losses. The size, shape and purity of nanoparticles have a significant impact on the magnetic properties of the particles employed in th recording media. For use with minimum recording media, the particles must have a single pure phase domain, high coercivity and medium magnetism [17].

The Co-Zn ferrites are also preferred due to their wide variety of applications and affordable price. Several studies have been done on the higher content of cobalt in zinc ferrite, but not much is known about the lower content of cobalt in

zinc ferrites. The structural investigation of cobalt mixed zinc ferrites for $x < 0.4$, as well as the magnetic and vibrational bond stretching properties are reported in present study.

EXPERIMENTAL

Ferric nitrate nonahydrate ($FeN_3O_9·9H_2O$, 98%) crystalline from Alfa Aesar, zinc nitrate hexahydrate ($Zn(NO_3)_2·6H_2O$, 99%) crystalline from Alfa Aesar, cobaltnitrate hexa hydrate ($Co(NO_3)_2·6H_2O$, 98%) crystalline from Alfa Aesar and citric acid ($C_6H_8O_7·H_2O$, 99.8%) Fizmerk, India, were used in powder form for the synthesis of cobalt doped zinc ferrite nanomaterial. The quantities of different reagents used for the distinct compositions are given in Table-1.

Synthesis of cobalt doped zinc ferrites: The cobalt doped zinc ferrite nanomaterial was prepared by the solution-gelation methods followed by auto combustion. In this process, a mixture of $Zn(NO_3)_2·6H_2O$, $Co(NO_3)_2·6H_2O$ and $Fe(NO_3)_3·9H_2O$ salts were mixed in 100 mL double deionized water with distinct composition as shown in Table-1 and 6.3042 g of citric acid was added to maintain the ratio of the fuel to the oxidizer ϕ = 1.35 [18]. The mixture was stirred in a beaker on a hot plate for 2 h at 80 ºC to get a uniform mixture. Dropwise ammonia solution (NH_4OH) was added to get the pH value by 7. Further, the hot plate was heated to achieve a temperature of 240 ºC. The solution slowly evaporated and transformed into gel form. This gel was later automatically combusted and converted into ash. After cooling to room temperature, the ash was crushed using a pestle and agate mortar to get it in fine particles form. These fine particles were calcined at 600 ºC in a muffle furnace for 4 h for being used to characterize.

RESULTS AND DISCUSSION

Structural analysis

Experimental XRD: The X-ray diffractogram of the prepared cobalt doped zinc ferrites were obtained by HRXRD (X'PertPro) in the range of 10-80º and are shown in Fig. 1. Different peaks are leveled to identify the phase of zinc ferrite, which are exactly matched with the JCPDS card No. 22-1012

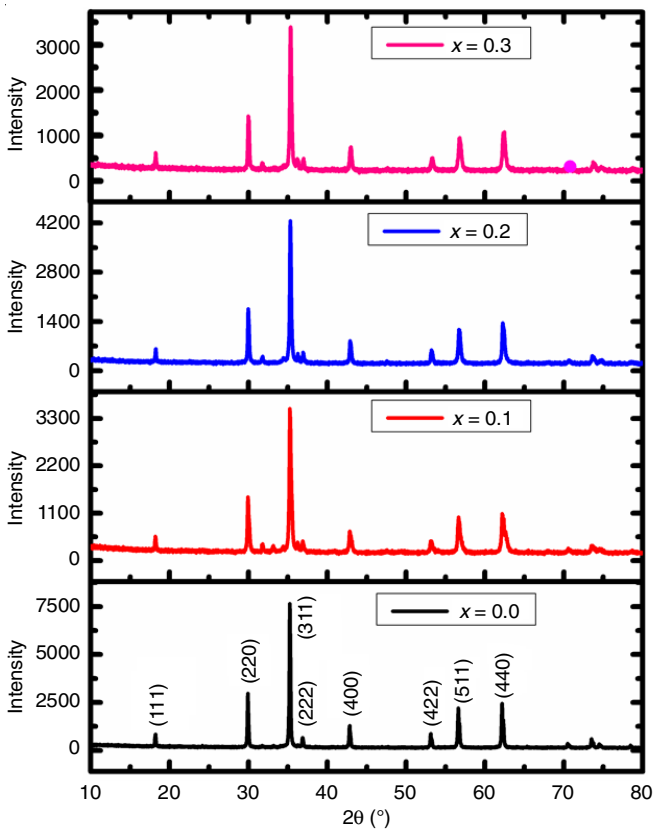

Fig. 1. XRD diffractogram of $Co_xZn_{1-x}Fe_2O_4$ (for x = 0.0, 0.1, 0.2, 0.3)

of $ZnFe_2O_4$ [19]. The sharp and intense peaks of X-ray diffraction spectra reveals that the samples have single phase with good crystalline nature. Entire reflections that appeared in diffraction patterns are in agreement with a single-phase cubic spinel structure with face-centered cubic geometry and represent the *Fd3m* space group. The Co-Zn ferrites contained no impurity peaks within the limit of the scanned range of X-ray detection. Crystallite size (D) and lattice parameter (a) for all compositions under investigation were calculated and presented in Table-2. Here, the lattice parameter (a) decreases as the doping level of cobalt increases, which indicates that some zinc ions of higher ionic radii are replaced by cobalt ions comparatively of lower ionic radii.

TABLE-1
AMOUNT OF ALL THE ESSENTIAL REAGENTS FOR PREPARATION of $Co_xZn_{1-x}Fe_2O_4$ NANOPARTICLES (x = 0.0, 0.1, 0.2 AND 0.3)

Reagents	x = 0.0	x = 0.1	x = 0.2	x = 0.3
$Co(NO_3)_2·6H_2O$	0 mol; 0 g	0.001 mol; 0.2910 g	0.002 mol; 0.5820 g	0.003 mol; 0.8730 g
$Zn(NO_3)_2·6H_2O$	0.01 mol; 2.9747 g	0.009 mol; 2.6772 g	0.008 mol; 2.3797 g	0.007 mol; 2.0822 g
$Fe(NO_3)_3·9H_2O$	0.02 mol; 8.08g	0.02 mol; 8.08g	0.02 mol; 8.08g	0.02 mol; 8.08g
Citric acid	0.03 mol; 6.3042 g	0.03 mol; 6.3042 g	0.03 mol; 6.3042 g	0.03 mol; 6.3042 g

TABLE-2
COMPOSITIONAL DEPENDENCE OF PHYSICAL PARAMETERS OF $Co_xZn_{1-x}Fe_2O_4$ NANOPARTICLES (x = 0.0, 0.1, 0.2 AND 0.3)

Compound	2θ (°)	FWHM	Crystallite size (D) (nm)	Interplaner distance (d) (Å)	Lattice parameter (a) (Å)	Volume (V) = a^3 (Å^3)
$ZnFe_2O_4$	35.24	0.1972	44.17	2.542	8.433	601.201
$Co_{0.1}Zn_{0.9}Fe_2O_4$	35.31	0.3336	26.11	2.539	8.423	597.746
$Co_{0.2}Zn_{0.8}Fe_2O_4$	35.34	0.2463	35.37	2.537	8.416	596.273
$Co_{0.3}Zn_{0.7}Fe_2O_4$	35.36	0.2727	31.95	2.536	8.412	595.294

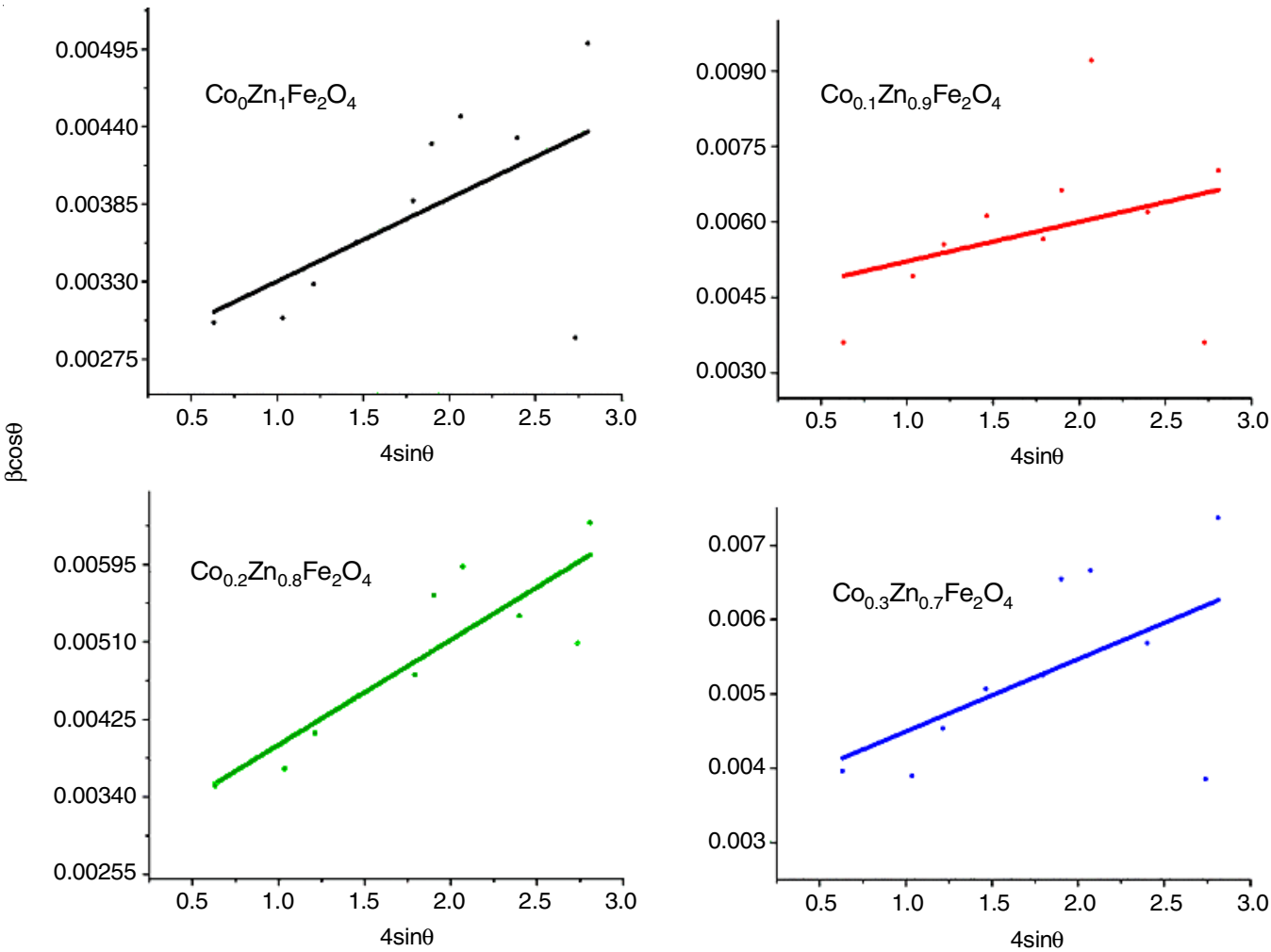

Fig. 2. Williamson-Hall plot of all the samples

The strain developed in the prepared materials were also calculated using the Williamson Hall (WH) formula:

$$\beta\cos\theta = \frac{0.9\lambda}{d} + 4\varepsilon\sin\theta$$

where β is full width at half maxima (FWHM), θ is the Bragg's angle, λ is the wavelength of used X-ray, d is the crystallite size and ε represents the intrinsic strain. The typical Williamson-Hall plots are shown in Fig. 2. Lattice strain has been calculated using the Williamson-Hall plot by taking the slope of the linear fit of the Williamson-Hall plot for each sample. Thus, it is determined that the lattice strain increases after Co incorporation into Zn ferrite, but then decreases as the percentage of Co increases as shown in Fig. 3.

An increase in the strain for $x = 0.1$ and 0.2 Co content as compared to Zn ferrite sample is due to increase in the concentration of increase in the imperfection of lattice. Moreover, the observed decrease in strain with increased Co content implies a corresponding decrease in the concentration of lattice imperfections, resulting in the preparation of high-quality samples.

Theoretical simulation: VESTA (OpenGL version: 3.3.0, Tsukuba, Japan), Material Project and Endeavor software were utilized for polyhedral, ball-stick and wireframe representation

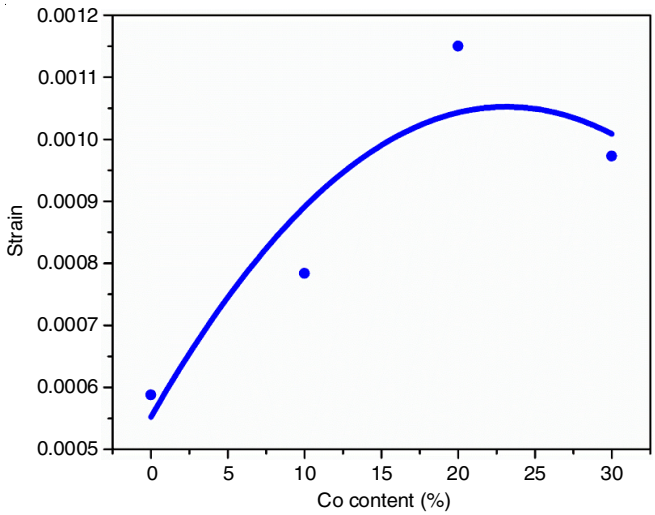

Fig. 3. Strain variation in $Co_xZn_{1-x}Fe_2O_4$

of different phases obtained in simulation studies [20]. All the theoretical structures were optimized using crystallography open database [21]. Furthermore, thorough investigations of the polycrystalline composite systems were performed by utilizing the experimental XRD diffraction pattern and Match3!

Software [22-26]. Theoretical simulation of base materials exhibited cubic system zinc ferrite $ZnFe_2O_4$ (Fig. 4), with lattice type F, space group *Fd3m* with space group number 227 and setting number two. For the unit cell of $ZnFe_2O_4$, $a = b = c =$ 8.44 Å and $\alpha = \beta = \gamma = 90°$. The unit cell volume of the system $ZnFe_2O_4$ was found to be 601.660 Å^3. The experimental XRD diffraction pattern was perfectly in agreement with simulation pattern of the composite which confirmed the single-phase formation of base materials $ZnFe_2O_4$. When 10% Co was added in pure base material $ZnFe_2O_4$, one new phase appeared to be hexagonal $Zn_{0.85}Co_{0.15}$ as a minor phase with lattice type P, space group P63mc with space group number 186 and setting number one. Inside the unit cell of $Zn_{0.85}Co_{0.15}$, $a = b = 3.25$, while $c = 5.204$ Å and $\alpha = \beta = 90°$ with $\gamma = 120°$. The unit cell volume of the system $ZnFe_2O_4$ was found to be 601.660 Å^3. At increasing proportion of Co to be 20%, two minor phases appeared to be $Zn_{0.85}Co_{0.15}$ and Co_2Zn_{11}, respectively. The crystal Co_2Zn_{11} emerged due to increasing percentage of cobalt in base material $ZnFe_2O_4$. Theoretical simulation exhibited Co_2Zn_{11}, to be cubic system with lattice type I, space group $I\bar{4}3m$ with space group number 217. Inside the unit cell of $ZnFe_2O_4$, $a = b = c = 8.96$ Å and $\alpha = \beta = \gamma = 90°$. The unit cell volume of the system $ZnFe_2O_4$ was found to be 720.624 Å^3. When the entitlement of Co is further increased to be 30%, the major phase $ZnFe_2O_4$ was replaced by $CoFe_2O_4$, which indicate that Zn was probably replaced by Co for the crystal system $ZnFe_2O_4$ while another minor phase was appeared to be $Zn_{0.85}Co_{0.15}$. Additionally, theoretical simulation exhibited $CoFe_2O_4$ to be trigonal system with lattice type R, space group $R\bar{3}m$, space group number 166 with setting number one (with hexagonal axes). Inside the unit cell of $CoFe_2O_4$, $a = b = 5.94$, $c = 14.54$ Å and $\alpha = \beta = 90°$, while $\gamma = 120°$. The unit cell volume of the system $ZnFe_2O_4$ was found to be 443.87 Å^3.

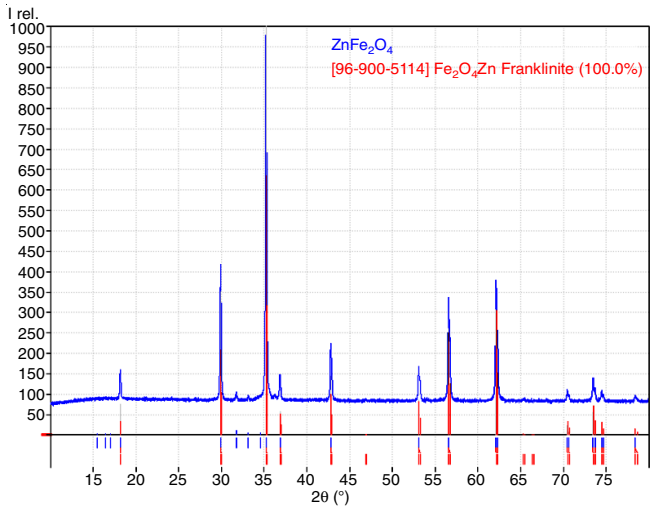

Fig. 4. Theoretical XRD pattern of $ZnFe_2O_4$

FTIR studies: The FTIR spectra of the synthesized Co-Zn ferrites nanomaterial were collected using Spectrum Two, Perkin-Elmer in the frequency range of 4000 to 400 cm^{-1} at 25 ºC. For FTIR spectroscopy, the Co-Zn ferrites and KBr pellets were mixed at a 1:20 ratio. Two absorption bands ν_1 and ν_2 were observed from the FTIR spectra near to 410.86 cm^{-1} and 544.62 cm^{-1}, signifying the intrinsic stretched vibrations between metal-oxygen at A and B sites, respectively [27-29] (Fig. 5). The peak of absorption band ν_3 near to1600 cm^{-1} is due to the stretching vibration of hydroxyl ion and broad band ν_4 near to 3400 cm^{-1} is due to the bending mode of H_2O molecule indicate the presence of water molecules on the surface of the prepared ferrite nanoparticles. The two strong peaks ν_1 and ν_2 (characteristic peaks of zinc ferrites) represents tetrahedral and octahedral modes of Co-Zn ferrites; this was assigned to Zn-O and Fe-O vibrations, respectively. Table-3 presents the bands recorded for the various compositions of Co-doped zinc ferrite.

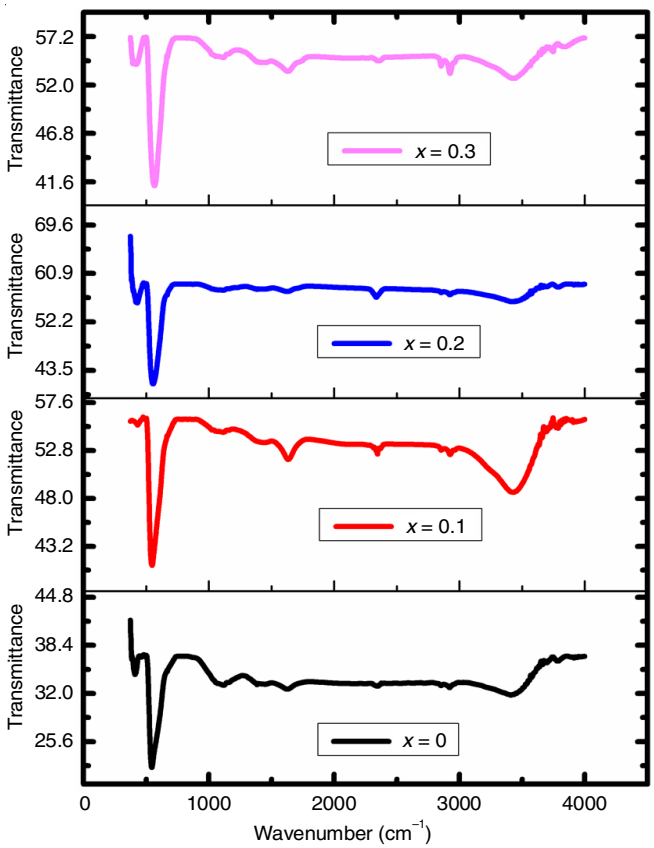

Fig. 5. FTIR spectra of of $Co_xZn_{1-x}Fe_2O_4$ (for $x = 0.0, 0.1, 0.2, 0.3$)

TABLE-3
ABSORPTION BANDS OF $Co_xZn_{1-x}Fe_2O_4$ NANOPARTICLES ($x = 0.0, 0.1, 0.2$ AND 0.3) AT ROOM TEMPERATURE

Sample	Peak ν_1 (cm^{-1})	Peak ν_2 (cm^{-1})	Peak ν_3 (cm^{-1})	Peak ν_4 (cm^{-1})
$ZnFe_2O_4$	410.86	544.62	1627.19	3414.52
$Co_{0.1}Zn_{0.9}Fe_2O_4$	431.13	547.32	1629.11	3423.74
$Co_{0.2}Zn_{0.8}Fe_2O_4$	428.91	554.49	1635.98	3424.34
$Co_{0.3}Zn_{0.7}Fe_2O_4$	415.68	565.46	1636.95	3432.35

SEM studies: The structural and morphological analysis of materials was carried out by SEM (MIRA TESCAN). SEM images of cobalt doped zinc ferrite nanomaterial for $x = 0.0$, 0.1, 0.2 and 0.3 are displayed in Fig. 6a-d. As can be seen from Fig. 6a that zinc ferrite shows particles with clear grain boundaries and throughout the sample surface the grains are almost spherical and homogeneously distributed. After incorp-

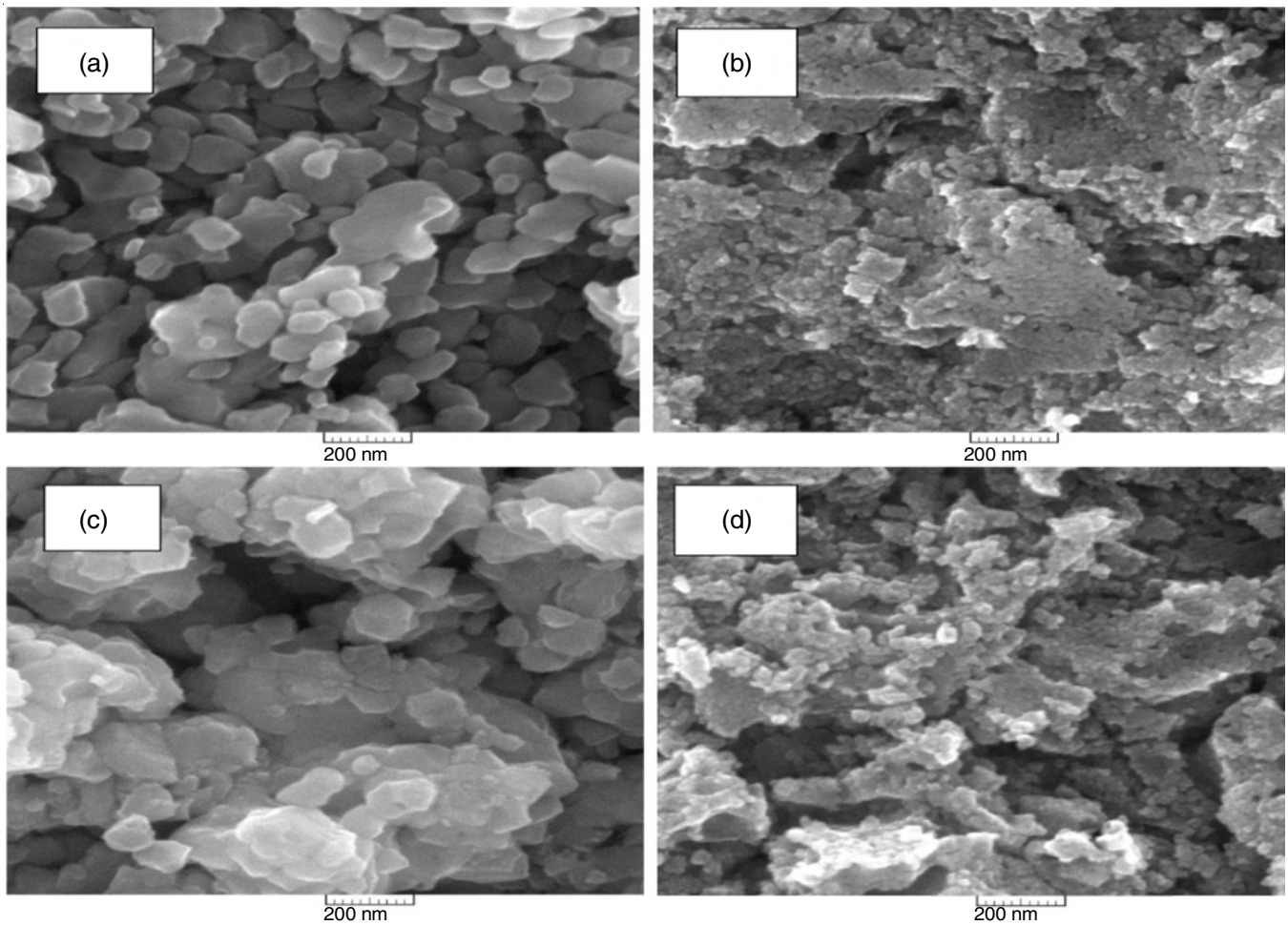

Fig. 6. SEM images of $Co_xZn_{1-x}Fe_2O_4$ (for x = 0.0, 0.1, 0.2, 0.3)

oration of Co ion in zinc ferrite matrix, particles are started to agglomerate (Fig. 6b) and further incorporation Co results in loss of visibility of the boundaries (Fig. 6c) because of their magnetic nature. Furthermore, pores can be seen in the highest percentage of the Co content in Zn ferrites as shown in Fig. 6d. Such porous morphological properties make it an effective material for humidity and gas sensing applications.

Magnetic property: The magnetic characteristics of the synthesized nanomaterial $Co_xZn_{1-x}Fe_2O_4$ (x = 0.0, 0.10, 0.20 and 0.30) were characterized using a vibrating sample magnetometer (VERSA LAB 3 TESLA CRYOGEN-FREE VSM) in the magnetizing intensity field range of -10 to +10 kOe at 25 ºC. According to prior observations [30], the value of magnetization rises linearly with the strength of the magnetic field from outside but is not yet saturated. Zn^{2+} and Fe^{3+} ions should be present in the tetrahedral (A) and octahedral (B) sites of as-synthesized Zn-Co ferrites, whereas Co^{2+} ions should be available in the favoured B sites [31-33]. According to the Stoner-Wohlfarth and Neel-Brown theories [34,35], the blocking temperature, nanocrystal volume and magneto crystalline anisotropy constant all influence the magnetic state of a nanocrystal. The strength of spin-orbital coupling at crystal lattices and the size of the crystal are both strongly associated with the magnitude of these [36]. The hysteresis curve (Fig. 7) demonstrates indisputably that the generated nanomaterial has a hard magnetic character, *i.e.* the magnetic material's domain walls do not move easily in the presence of a magnetic field. Additionally, the plot clearly shows that the saturation magnetization rises continuously with cobalt content.

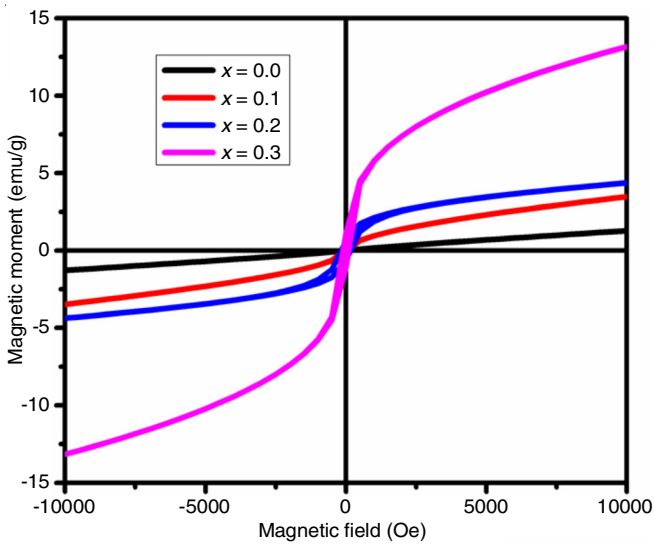

Fig. 7. Hysteresis loop of $Co_xZn_{1-x}Fe_2O_4$ (for x = 0.0, 0.1, 0.2, 0.3)

The synthesized nanomaterial exhibits paramagnetic properties for $x = 0.0$. Their nanoscale size reduction, which causes a divergence from their expected structure, as well as an unbalance of Fe^{3+} ions on octahedral and tetrahedral sites in the crystal structure, are likely explanations of this behaviour. Generally, the coercivity increases with cobalt presence. Table-4 presents the several parameters that were extracted from this plot. The hysteresis curve shows that even for high magnetizing intensities, the composition with a higher cobalt concentration displays behaviour resembling unsaturation. The atomic surface layer's spin disorder is to blame for this [37].

TABLE-4
MAGNETIC PARAMETERS DATA OF $Co_xZn_{1-x}Fe_2O_4$ NANO-PARTICLES (x = 0.0, 0.1, 0.2 and 0.3) AT ROOM TEMPERATURE

Co conc. (x)	Saturation magnetization, M_S (emu/g)	Remanence, M_r (emu/g)	Coercivity, H_c (Oe)	Reduced remanence $S = M_r/M_S$
0.0	1.2880	0.0061	35.7640	0.0048
0.1	3.4712	0.0847	58.2749	0.0244
0.2	4.4139	0.6127	168.2071	0.1388
0.3	13.1466	1.1102	103.3025	0.0844

Conclusion

Cobalt-doped nano zinc ferrites were prepared by the solution gelation processes followed by self-ignition. PXRD, FTIR, SEM and VSM techniques were applied for the characterization of the synthesized nanoparticles. The PXRD pattern reveals that the synthesized nanoparticles have a cubic spinel ferrite phase with space group *Fd3m*. The doping of cobalt decreases the lattice constant from 8.4471 Å to 8.4175 Å and reduces the crystallite size from 50.249 nm to 27.561 nm. Additionally, the doping of cobalt, affected the variation in the elemental compositions of composite systems as shown in theoretical XRD and cobalt have appeared with higher concentration as it was increased in the prepared nanomaterial respectively and for 30% content of cobalt the major phase $ZnFe_2O_4$ was replaced by $CoFe_2O_4$. The hysteresis curve amply demonstrates the hard magnetic nature of the synthesized nanomaterial and exhibits unsaturation behaviour for $x = 0.3$ even in the presence of a strong magnetic field.

ACKNOWLEDGEMENTS

The authors are thankful to Department of Physics, Uma Nath Singh Institute of Engineering and Technology, V.B.S. Purvanchal University, Jaunpur; Raja Ramanna Centre for Advanced Technology, Indore; and Inter-University Accelerator Centre (IUAC), New Delhi, India for providing the sophisticated instrumentation facilities.

CONFLICT OF INTEREST

The authors declare that there is no conflict of interests regarding the publication of this article.

REFERENCES

1. Q. Song and Z.J. Zhang, *J. Am. Chem. Soc.*, **126**, 6164 (2004); https://doi.org/10.1021/ja049931r
2. W. Bayoumi, *J. Mater. Sci.*, **42**, 8254 (2007); https://doi.org/10.1007/s10853-007-1616-8
3. P.C. Morais, V.K. Garg, A.C. Oliveira, L.P. Silva, R.B. Azevedo, A.M.L. Silva and E.C.D. Lima, *J. Magn. Magn. Mater.*, **225**, 37 (2001); https://doi.org/10.1016/S0304-8853(00)01225-7
4. A. Manikandan, L.J. Kennedy, M. Bououdina and J.J. Vijaya, *J. Magn. Magn. Mater.*, **349**, 249 (2014); https://doi.org/10.1016/j.jmmm.2013.09.013
5. C. Singh, S. Jauhar, V. Kumar, J. Singh and S. Singhal, *Mater. Chem. Phys.*, **156**, 188 (2015); https://doi.org/10.1016/j.matchemphys.2015.02.046
6. G. Fan, J. Tong and F. Li, *Ind. Eng. Chem. Res.*, **51**, 13639 (2012); https://doi.org/10.1021/ie201933g
7. S.-K. Chang, Z. Zainal, K.-B. Tan, N.A. Yusof, W.M.D. Wan Yusoff and S.R.S. Prabaharan, *Int. J. Energy Res.*, **39**, 1366 (2015); https://doi.org/10.1002/er.3339
8. D.K. Pawar, J.S. Shaikh, B.S. Pawar, S.M. Pawar, P.S. Patil and S.S. Kolekar, *J. Porous Mater.*, **19**, 649 (2012); https://doi.org/10.1007/s10934-011-9516-3
9. I.C. Nlebedim, M. Vinitha, P.J. Praveen, D. Das and D.C. Jiles, *J. Appl. Phys.*, **113**, 193904 (2013); https://doi.org/10.1063/1.4804963
10. X. Huang, J. Zhang, S. Xiao and G. Chen, *J. Am. Ceram. Soc.*, **97**, 1363 (2014); https://doi.org/10.1111/jace.12909
11. X. Yang, Q. Jin, Z. Chen, Q. Li and B. Liu, *J. Magn. Magn. Mater.*, **367**, 64 (2014); https://doi.org/10.1016/j.jmmm.2014.04.053
12. N.A. Spaldin, *Proc. R. Soc. A*, **476**, 20190542 (2020); http://dx.doi.org/10.1098/rspa.2019.0542
13. C. Lu, M. Wu, L. Lin and J.-M. Liu, *National Sci. Rev.*, **6**, 653 (2019); https://doi.org/10.1093/nsr/nwz091
14. M. Bichurin, V. Petrov, S. Priya and A. Bhalla, *Adv. Condensed Matt. Phys.*, **2012**, 129794 (2012); https://doi.org/10.1155/2012/129794
15. F. Sharifianjazi, M. Moradi, N. Parvin, A. Nemati, A.J. Rad, N. Sheysi, M. Irani, A. Abouchenari, S. Sahmani, A. Mohammadi, S. Karbasi, Z. Ahmadi, A. Esmaeilkhanian, A. Pakseresht and M.S. Asl, *Ceram. Int.*, **46**, 18391 (2020); https://doi.org/10.1016/j.ceramint.2020.04.202
16. S.J. Salih and W.M. Mahmood, *Heliyon*, **9**, e16601 (2023); https://doi.org/10.1016/j.heliyon.2023.e16601
17. Q. Li, C.W. Kartikowati, S. Horie, T. Ogi, T. Iwaki and K. Okuyama, *Sci. Rep.*, **7**, 9894 (2017); https://doi.org/10.1038/s41598-017-09897-5
18. Feng J, Xiong R, Liu Y, Su F, Zhang X., *J. Mater. Sci: Mater. Electron.*, **29**, 18358 (2018); https://doi.org/10.1007/s10854-018-9950-y
19. A. Manikandan, J. Judith Vijaya, M. Sundararajan, C. Meganathan, L.J. Kennedy and M. Bououdina, *Superlattices Microstruct.*, **64**, 118 (2013); https://doi.org/10.1016/j.spmi.2013.09.021
20. Shweta, S.K. Avinashi, A. Hussain, Z. Fatima, K. Sharma, S. Khanka, R. Prakash, D. Singh and C. Gautam, *Ceram. Int.*, **48**, 8801 (2022); https://doi.org/10.1016/j.ceramint.2022.11.031
21. S.K. Avinashi, P. Singh, Shweta, K. Sharma, A. Hussain, D. Singh and C. Gautam, *Ceram. Int.*, **48**, 18475 (2022); https://doi.org/10.1016/j.ceramint.2022.03.117
22. R.K. Mishra, D. Gupta, S.K. Avinashi, S. Kumari, A. Hussain and C. Gautam, *Silicon*, **15**, 2567 (2022); https://doi.org/10.1007/s12633-022-02196-3
23. A. Gautam, C. Gautam, M. Mishra, V.K. Mishra, A. Hussain, S. Sahu, R. Nanda, B. Kisan, S. Biradar and R.K. Gautam, *RSC Adv.*, **9**, 40977 (2019); https://doi.org/10.1039/C9RA07835E
24. Z. Fatima, A. Hussain, C. Gautam, Shweta, P. Singh, A. Ahmed, G. Singh and M.K. Singh, *J. Asian Ceram. Soc.*, **8**, 1108 (2020); https://doi.org/10.1080/21870764.2020.1815349
25. A. Hussain, C. Gautam, A. Jafri, V.K. Mishra, A. Madheshiya, A. Gautam, M.K. Singh, R.K. Gautam, M. Gupta, M. Arshad, R. Vajtai and P.M. Ajayan, *Ceram. Int.*, **46**, 23006 (2020); https://doi.org/10.1016/j.ceramint.2020.06.077

26. S.K. Avinashi, A. Hussain, K. Kumar, B.C. Yadav and C. Gautam, *Oxford Open Mater. Sci.*, **1**, itab006 (2021); https://doi.org/10.1093/oxfmat/itab006
27. S. Maensiri, C. Masingboon, B. Boonchom and S. Seraphin, *Scr. Mater.*, **56**, 797 (2007); https://doi.org/10.1016/j.scriptamat.2006.09.033
28. R. Roshani and A. Tadjarodi, *J. Mater. Sci. Mater. Electron.*, **31**, 23025 (2020); https://doi.org/10.1007/s10854-020-04830-5
29. F. Gönen and G. Tekinerdogan, *J. Nanotechnol.*, **2020**, 3139701 (2020); https://doi.org/10.1155/2020/3139701
30. F. Li, H. Wang, L. Wang and J. Wang, *J. Magn. Magn. Mater.*, **309**, 295 (2007); https://doi.org/10.1016/j.jmmm.2006.07.012
31. V. Blanco-Gutierrez, E. Climent-Pascual, M.J. Torralvo-Fernandez, R. Saez-Puche and M.T. Fernandez-Diaz, *J. Solid State Chem.*, **184**, 1608 (2011); https://doi.org/10.1016/j.jssc.2011.04.034
32. V. Blanco-Gutierrez, F. Jiménez-Villacorta, P. Bonville, M.J. Torralvo-Fernández and R. Sáez-Puche, *J. Phys. Chem. C*, **115**, 1627 (2011); https://doi.org/10.1021/jp109368z
33. V. Blanco-Gutierrez, M.J. Torralvo-Fernández and R. Sáez-Puche, *J. Phys. Chem. C*, **114**, 1789 (2010); https://doi.org/10.1021/jp908395v
34. E.C. Stoner and E.P. Wohlfarth, *Trans. R. Soc.*, **A240**, 599 (1948); https://doi.org/10.1098/rsta.1948.0007
35. W.F. Brown, *Phys. Rev.*, **130**, 1677 (1963); https://doi.org/10.1103/PhysRev.130.1677
36. Q. Song and Z.J. Zhang, *J. Phys. Chem. B*, **110**, 11205 (2006); https://doi.org/10.1021/jp060577o
37. M.A. Rahman, M.T. Islam, M.S.J. Singh, M. Samsuzzaman and M.E.H. Chowdhury, *Sci. Rep.*, **11**, 7654 (2021); https://doi.org/10.1038/s41598-021-87100-6